Radial velocity follow-up of GJ1132 with HARPS

X. Bonfils, J.-M. Almenara, R. Cloutier, A. Wünsche, N. Astudillo-Defru, Z. Berta-Thompson, F. Bouchy, D. Charbonneau, X. Delfosse, R. F. Díaz, et al.

A&A 618, A142 (2018)
https://doi.org/10.1051/0004-6361/201731884

Astronomy & Astrophysics

Radial velocity follow-up of GJ1132 with HARPS⋆,⋆⋆

A precise mass for planet b and the discovery of a second planet

X. Bonfils[1], J.-M. Almenara[1], R. Cloutier[3,4,5], A. Wünsche[1], N. Astudillo-Defru[2,6], Z. Berta-Thompson[7], F. Bouchy[2], D. Charbonneau[8], X. Delfosse[1], R. F. Díaz[10,11], J. Dittmann[9], R. Doyon[5], T. Forveille[1], J. Irwin[8], C. Lovis[2], M. Mayor[2], K. Menou[3], F. Murgas[14,15], E. Newton[9], F. Pepe[2], N. C. Santos[12,13], and S. Udry[2]

[1] Université Grenoble Alpes, CNRS, IPAG, 38000 Grenoble, France
[2] Observatoire de Genève, Université de Genève, 51 ch. des Maillettes, 1290 Sauverny, Switzerland
[3] Department of Astronomy & Astrophysics, University of Toronto, 50 St. George Street, M5S 3H4 Toronto, Canada
[4] Centre for Planetary Sciences, Department of Physical & Environmental Sciences, University of Toronto Scarborough, 1265 Military Trail, M1C 1A4 Toronto, Canada
[5] Institut de Recherche sur les Exoplanètes, Département de physique, Université de Montréal, CP 6128 Succ. Centre-ville, H3C 3J7 Montréal, Canada
[6] Departamento de Astronomía, Universidad de Concepción, Casilla 160, Concepción, Chile
[7] Department of Astrophysical and Planetary Sciences, University of Colorado, 2000 Colorado Ave., Boulder, CO 80305, USA
[8] Harvard-Smithsonian Center for Astrophysics, 60 Garden Street, Cambridge, MA 02138, USA
[9] Kavli Institute for Astrophysics and Space Research, Massachusetts Institute of Technology, 77 Massachusetts Avenue, Cambridge, MA 02139, USA
[10] Facultad de Ciencias Exactas y Naturales, Universidad de Buenos Aires, Buenos Aires, Argentina
[11] CONICET – Universidad de Buenos Aires. Instituto de Astronomía y Física del Espacio (IAFE), Buenos Aires, Argentina
[12] Instituto de Astrofísica e Ciências do Espaço, Universidade do Porto, CAUP, Rua das Estrelas, 4150-762 Porto, Portugal
[13] Departamento de Física e Astronomia, Faculdade de Ciências, Universidade do Porto, Rua do Campo Alegre, 4169-007 Porto, Portugal
[14] Instituto de Astrofśica de Canarias (IAC), 38200 La Laguna, Tenerife, Spain
[15] Departamento de Astrofísica, Universidad de La Laguna (ULL), 38206 La Laguna, Tenerife, Spain

Received 1 September 2017 / Accepted 4 June 2018

ABSTRACT

The source GJ1132 is a nearby red dwarf known to host a transiting Earth-size planet. After its initial detection, we pursued an intense follow-up with the HARPS velocimeter. We now confirm the detection of GJ1132b with radial velocities alone. We refined its orbital parameters, and in particular, its mass (m_b = 1.66 ± 0.23 $M_\oplus$), density (ρ_b = 6.3 ± 1.3 g cm^{-3}), and eccentricity (e_b < 0.22; 95%). We also detected at least one more planet in the system. GJ1132c is a super-Earth with period P_c = 8.93 ± 0.01 days and minimum mass $m_c \sin i_c$ = 2.64 ± 0.44 $M_\oplus$. Receiving about 1.9 times more flux than Earth in our solar system, its equilibrium temperature is that of a temperate planet ($T_{\rm eq}$ = 230−300 K for albedos A = 0.75 − 0.00), which places GJ1132c near the inner edge of the so-called habitable zone. Despite an a priori favorable orientation for the system, *Spitzer* observations reject most transit configurations, leaving a posterior probability <1% that GJ1132c transits. GJ1132(d) is a third signal with period P_d = 177 ± 5 days attributed to either a planet candidate with minimum mass $m_d \sin i_d = 8.4^{+1.7}_{-2.5}$ $M_\oplus$ or stellar activity. Its Doppler signal is the most powerful in our HARPS time series but appears on a timescale where either the stellar rotation or a magnetic cycle are viable alternatives to the planet hypothesis. On the one hand, the period is different than that measured for the stellar rotation (~125 days), and a Bayesian statistical analysis we performed with a Markov chain Monte Carlo and Gaussian processes demonstrates that the signal is better described by a Keplerian function than by correlated noise. On the other hand, periodograms of spectral indices sensitive to stellar activity show power excess at similar periods to that of this third signal, and radial velocity shifts induced by stellar activity can also match a Keplerian function. We, therefore, prefer to leave the status of GJ1132(d) undecided.

Key words. techniques: radial velocities – stars: late-type – planetary systems

⋆ Based on observations made with the HARPS instrument on the ESO 3.6 m telescope under the program IDs 191.C-0873(A), and 198.C-0838(A), at Cerro La Silla (Chile).
⋆⋆ Radial velocity data are only available at the CDS via anonymous ftp to cdsarc.u-strasbg.fr (130.79.128.5) or via http://cdsarc.u-strasbg.fr/viz-bin/qcat?J/A+A/618/A142

1. Introduction

The source GJ1132 is an M dwarf of our solar neighborhood with a known transiting planet detected by the MEarth survey (Berta-Thompson et al. 2015). Owing to the small size, low mass, and low temperature of the parent star (~0.21 $R_\odot$, 0.18 $M_\odot$, and 3 300 K), the 1.6-day periodic, 2.6 mmag dips observed in its photometric light curves imply that the planet has a size comparable to that of Earth (~1.2 $R_\oplus$) and a warm equilibrium temperature (~400–600 K). Being 2–3 mag brighter than most other Earth-size planet hosts detected with Kepler, for example, GJ1132 is an appealing system for follow-up characterization (Morley et al. 2017; Southworth et al. 2017).

The discovery paper already includes a radial-velocity (RV) time series collected with the HARPS spectrograph. With an orbital model composed of a single planet and a fixed zero eccentricity, we measured an orbital semi-amplitude of $2.76 \pm 0.92\,\mathrm{m\,s^{-1}}$, corresponding to a planetary mass of $1.62 \pm 0.55\,M_\oplus$ (Berta-Thompson et al. 2015). Although this favors a rocky composition, the constraint is loose given the large mass uncertainty to the point that even a gaseous composition remains possible in a 3σ range. In addition to bulk composition, the mass of the planet is also an important parameter for determining the scale height of the atmosphere and constrain transmission spectroscopy observations (Schaefer et al. 2016; Southworth et al. 2017).

If a better mass measurement already makes a strong case for pursuing an intensive RV follow-up, searching for additional planets is an equally good motivation. With a known transiting planet, we know the system is favorably aligned, and that additional planets have a high chance of being detected in transit as well (Gillon et al. 2011, 2017). The source GJ1132 has recently been used in simulations as an illustrative example of such a strategy (Cloutier et al. 2017b).

This paper reports on our RV follow-up campaign on GJ1132 with the HARPS spectrograph. We identify a first component with period $P_d = 177 \pm 5$ days that we attribute to either an outer planet with mass $m_d \sin i = 8.4^{+1.7}_{-2.5}\,M_\oplus$ or stellar activity. After subtracting this first signal, we show that GJ1132b is now identified with the sole RV data. Our time series then reveals another planet with mass $m_c \sin i_c = 2.7 \pm 0.4\,M_\oplus$ and period $P_c = 8.92 \pm 0.01$ days. With an equilibrium temperature of 230–300 K, this super-Earth is located near the habitable zone. Matching our ephemeris with *Spitzer* observations from Dittmann et al. (2017a), we found that unfortunately, transits of planet *c* are largely excluded.

2. Data

From June 6, 2015 (BJD = 2457180.5) to June 21, 2017 (BJD = 2457925.5), we collected 128 observations with the HARPS spectrograph (Mayor et al. 2003; Pepe et al. 2004), including the 25 measurements previously published in Berta-Thompson et al. (2015). We chose the high-resolution mode (R = 115 000), and used the scientific fiber for the target and the calibration fiber for the sky. In practice, the sky brightness is low enough and the second fiber is not used by our pipeline. It only serves as a potential a posteriori diagnostic. Exposure times were fixed to 40 min, except for one exposure on June 26, 2016 (BJD = 2457566.5), which was shortened to 1700 s. We also note that we discarded a 129th measurement that is found in ESO archives. It measured only 5 s and was taken on June 11, 2015 (BJD = 2457185.5).

The online pipeline produces extracted spectra that are calibrated in wavelength (Lovis & Pepe 2007). It also computes RVs through cross-correlation with a numerical mask (Baranne et al. 1996; Pepe et al. 2002). We used this initial estimate to shift all spectra to a common reference frame, and we coadded them to build a reference spectrum with a high signal-to-noise ratio (S/N). We then refined the RV determination by finding the best-fit Doppler shift between this reference template and individual spectra (e.g., Howarth et al. 1997; Galland et al. 2006; Anglada-Escudé & Butler 2012; Astudillo-Defru et al. 2015).

The RV uncertainties were evaluated by measuring the Doppler information content in the $\chi^2(RV)$ profile, using the formalism of Bouchy et al. (2001); Boisse et al. (2010). This formalism quantifies the RV uncertainty thorugh a weighted sum over the spectral elements with more weight given to the spectral elements with a higher derivative. Because the derivative of a spectrum has a higher variability against noise than the spectrum itself, we instead directly applied the formula to the $\chi^2(RV)$ profile, whose S/N is a few hundred times higher. For GJ1132, a V = 13.5 mag star, we estimate that photon noise contributes with 2–3 $\mathrm{m\,s^{-1}}$ to the precision of individual measurements.

In addition to RVs, we also measured several activity proxies such as spectroscopic indices (H_α, H_β, calcium S index, and Na; see Astudillo-Defru et al. 2017). Spectroscopic indices can reveal and trace inhomogeneities at the surface of the star, which, animated by the stellar rotation, can contribute to an apparent Doppler shift that is unrelated to the presence of planets (Bonfils et al. 2007; Robertson et al. 2014). Our time series for the RVs, their uncertainties, and the time series for the activity proxies are reported in Table A.1.

3. Analysis

3.1. Iterative periodogram analysis

We started with the RV time series (Fig. 1a) and computed its generalized Lomb–Scargle periodogram (Fig. 1b; Press et al. 1992; Zechmeister & Kürster 2009). We chose a normalization such that a power of 1 at a given period means that a sin-wave fit to the data is a perfect fit (χ^2 = 1), and a power of 0 means that a sin-wave fit does not improve the χ^2 over that of a fit by a constant. We identify several peaks with a high power: one at the period of the known planet GJ1132b (~1.63 day), one near the period 8.9 day, and, the strongest, around 171 days. They have a power p = 0.25, 0.26, and 0.30, respectively.

To evaluate the significance as a function of the power excess that is measured, we created synthetic data illustrative of time series with noise alone. To preserve the sampling, the simulated time series had the same dates as the original. To preserve the distribution of RVs around their mean, the values were picked by randomly shuffling the original time series. We computed the periodogram of simulated time series and measured their power maxima. After many trials, we built a distribution of power maxima that served as comparison with the power values measured in the original time series. We found that over 10 000 trials, no simulated time series has power maxima equal to or higher than p = 0.30, meaning that the peak detected around P = 177 day has a false-alarm probability (FAP) lower than 1/10 000 = 0.01%; it is equivalent to a significance >3.8σ.

We note that Berta-Thompson et al. (2015) found a rotation period of 125 days and that a sampling rate of ~1 yr could produce an alias at the period 190 day, which is indistinguishable from the 171-day peak. Nevertheless, the signal appears well

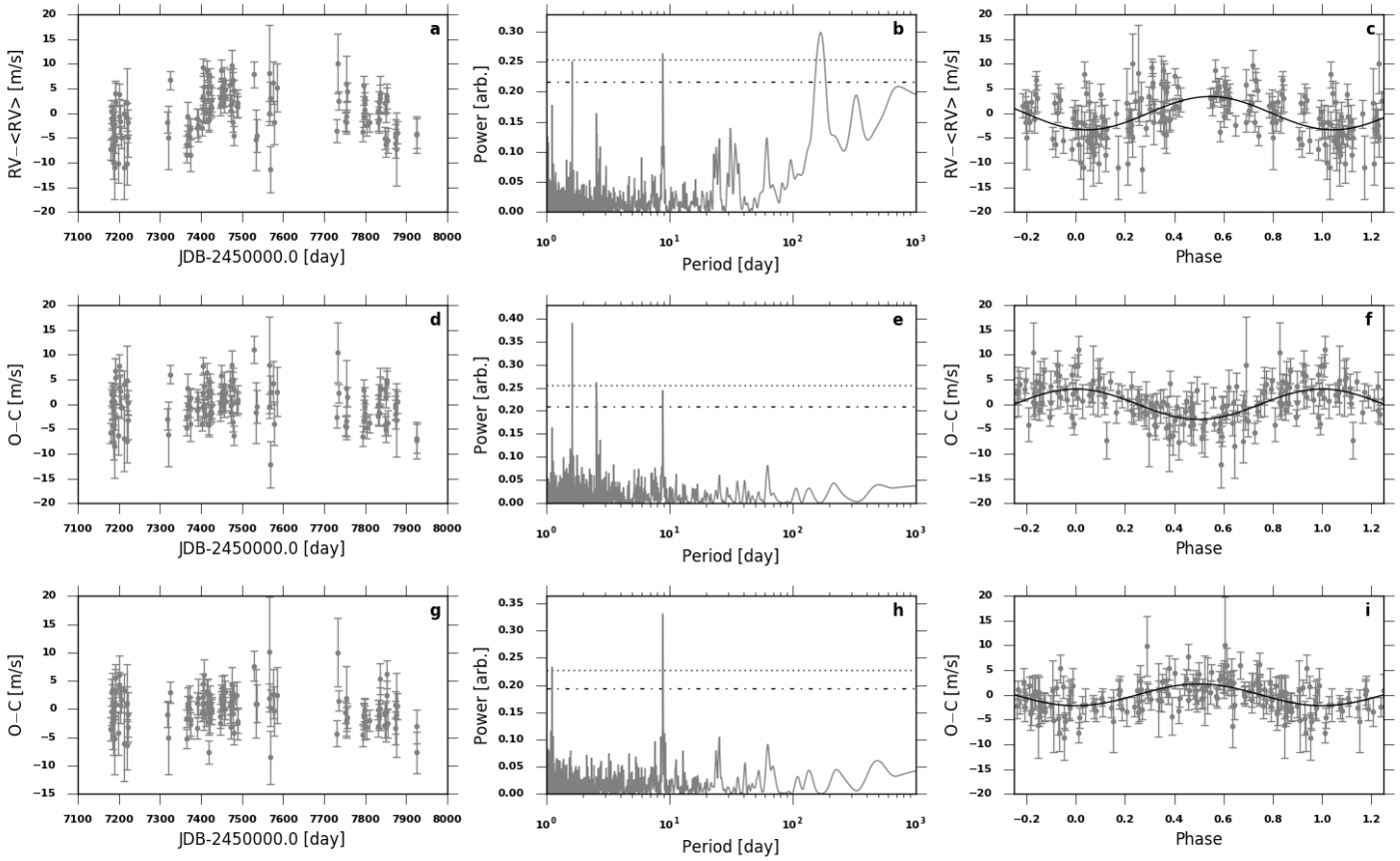

Fig. 1. Iterative periodogram analysis. *Left column:* RV times series before any subtraction (*panel a*), after subtracting a one-Keplerian fit (*panel d*) and after subtraction of a two-Keplerian fit (*panel g*). *Middle column:* periodograms for each RV time series in the left column. *Right column:* RV time series shown in the left column phase-folded to the period of maximum power shown in the periodograms of the middle column. The best sine fit is superimposed. Dash-dotted (resp. dotted) lines in *panels b*, *e*, and *h* are placed at a power level corresponding to a false-alarm probability of 1% (resp. 0.1%).

sampled when phased with a period of 177 or 190 days, and the 177-day peak is therefore probably not an alias.

We next reproduced the same periodogram analysis with spectroscopic indices. Figure 2 shows these periodograms for Ca (blue), Na (green), H_β (red), and H_α (cyan). The period of the stellar rotation is shown with the vertical full line, and the periods of the three Doppler signals discussed in this paper are shown with vertical dashed lines. Broad power excess is visible between 80–300 day, with a highest peak at the period of the stellar rotation (~125 day). Peaks of power are also visible near 175 day, calling for caution in interpreting the corresponding Doppler signal. If it is not due to stellar rotation, a magnetic cycle can also induce periodic variations (Gomes da Silva et al. 2011). In Sect. 3.2, we perform a more detailed modeling using Markov chain Monte Carlo (MCMC) and Gaussian processes algorithms. By statistically comparing models, we show that the signal is best described by a Keplerian, not by correlated noise. Nevertheless, since stellar activity can produce RV variations that match a Keplerian (Bonfils et al. 2007), we do not consider this comparison to clearly favor the planet interpretation.

We fit and removed a Keplerian component from the RVs and studied the residuals (Fig. 1d). The most prominent peak is now that of GJ1132b, and the RV residuals are well modeled by a Keplerian with period P = 1.63 day (Fig. 1f). The peak itself has an FAP lower than 0.01%. The detection is now significant even without prior knowledge of the period from the photometric transits. GJ1132b is therefore confirmed based on RV data alone.

We continued with a model composed of two Keplerian orbits. The residuals now show strong power excess around P = 8.9 days (FAP < 0.01%; Fig. 1g), which is also well modeled with an additional Keplerian (Fig. 1i).

The rotation measured for GJ1132 is clearly distinct from the last two RV periodicities. This meas that stellar activity is probably not responsible for these two short-period signals. We attribute them instead to two orbiting planets, namely, GJ1132b and c.

3.2. Joint modeling of planets and correlated "noise"

Here, we apply a second, complementary analysis to the data using al non-parametric Gaussian process (GP) regression model of the correlated RV residuals. GP regression modeling works within a Bayesian framework and provides a distribution of functions that model the correlations between adjacent RV measurements following the removal of a mean planetary model containing up to three planets in our analysis. This technique has recently been used in the literature to model stellar RV activity, thus facilitating the detection and precise characterization of planets around active stars (e.g., Haywood et al. 2014; Rajpaul et al. 2015; Donati et al. 2016; Cloutier et al. 2017b; Bonfils et al. 2018). A complete description of the techniques used to simultaneously model the RV variations with a GP plus Keplerian orbital solutions can be found in Cloutier et al. (2017a). Here, we briefly summarize the key steps and assumptions used in this work.

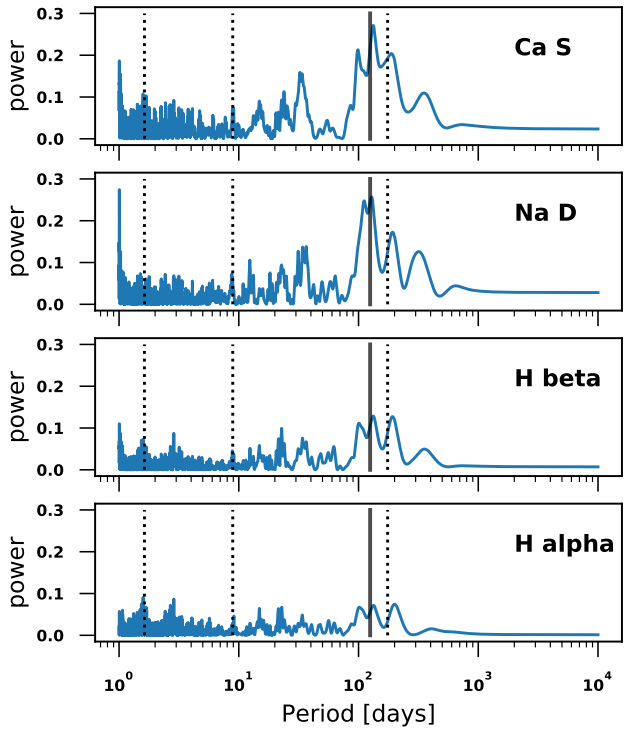

Fig. 2. Periodogram of spectral indices measured on HARPS spectra. Ca, Na, H_β, and H_α are shown from *top to bottom*. The period of the stellar rotation is shown with a vertical full line, and the periods of the three Doppler signals attributed to GJ1132b, GJ1132c, and GJ1132(d) are shown with vertical dashed lines.

We described above that the broad peak centered around ~175 days in the LS periodogram of the RVs spans the stellar photometric rotation period of 125 days (Dittmann et al. 2017a). Therefore, the stellar activity might be modulated at approximately the stellar rotation timescale. Thus, we adopted a quasi-periodic covariance kernel for the GP activity model of the form

$$k_{i,j} \propto \exp\left[-\frac{|t_i - t_j|^2}{2\lambda^2} - \Gamma^2 \sin^2\left(\frac{\pi|t_i - t_j|}{P_{\rm GP}}\right)\right], \quad (1)$$

where t_i is the ith BJD in the time series for $i, j = 1, \ldots, 128$. The GP hyperparameters a, λ, Γ, and $P_{\rm GP}$ describe the amplitude of the correlations, the exponential decay timescale, the coherence scale of the correlations, and the periodic timescale ($P_{\rm GP} = P_{\rm rot}$ in photometry), respectively. Because the GP is intended to only model the stellar activity, the posterior probability density functions (PDFs) of the four hyperparameters are trained through an MCMC on a training set that is independent of planetary signals. For this purpose, we used `emcee` (Foreman-Mackey et al. 2013), a `python` implementation of the affine-invariant ensemble MCMC sampler (Goodman & Weare 2010). We opted for a training set using the MEarth photometry presented in Berta-Thompson et al. (2015) that was used in Cloutier et al. (2017b) to model the stellar RV activity using a GP. Here, a well-defined solution is easily found, whose periodic term is the photometric rotation period. The resulting marginalized posterior PDFs of the GP hyperparameters λ, Γ, and $P_{\rm GP}$ are then used as priors when next we jointly modeled the RVs simultaneously with planetary signals and a quasi-periodic GP. The posterior PDFs of these three hyperparameters from training are each approximated by a one-dimensional kernel density estimation, which can then be sampled during the RV modeling. The covariance amplitude a was left as an effectively unconstrained free parameter in the RV modeling.

Table 1. Maximum ln $\mathcal{L}$ ratios for various competing models.

Model comparisons			ln-likelihood ratio
3 Keplerians	vs.	2 Keplerians	9e17 (>8σ)
2 Keplerians + GP	vs.	2 Keplerians	7e13 (7.6σ)
3 Keplerians	vs.	2 Keplerians + GP	1e4 (3.9σ)
3 Keplerians + GP	vs.	2 Keplerians + GP	1e5 (4.4σ)
3 Keplerians	vs.	3 Keplerians + GP	1.34 (0.3σ)

We then modeled the RVs with one of four potential planetary models. The first model contained the two planets GJ1132b and GJ1132c. The second model contained the same two planets plus the quasi-periodic GP. The third model assumed three planets, GJ1132b, GJ1132c, and GJ1132(d). The fourth model contained the same three planets plus the quasi-periodic GP. In each considered model, the orbital period and time of mid-transit of GJ 1132b were assigned Gaussian priors based on the transit results from Berta-Thompson et al. (2015). The orbital period of the putative GJ1132c (GJ1132(d)) was assigned a uniform prior between 8.8 and 9.0 days (between 120 and 220 days). We adopted uninformative Jeffreys priors between 0–10 m s^{-1} on the semi-amplitude of each planet. This choice of prior was modified and not found to significantly affect the results. The eccentricities e of each planet were sampled indirectly via the jump parameters $h = \sqrt{e}\cos\omega$ and $k = \sqrt{e}\sin\omega$, where ω is the argument of periastron. This choice reduces bias toward high eccentricities (Ford 2006).

Next, we conducted a model comparison using time-series cross-validation (Arlot & Celisse 2010). This procedure is computationally less expensive than computing the fully marginalized Bayesian likelihood and is independent of the choice of model parameter priors. The unique model parameters for each model, including the GP hyperparameter, were optimized for each of the 107 training sets, which contained between 20 and the full dataset size, less 1 (i.e., 127), chronologically spaced RV measurements. For each split of the data, the testing set was the single measurement taken after the final measurement in the training set. The ln-likelihood (ln $\mathcal{L}$) of the testing data given each model optimized on the training set were then computed. Over the 107 splits of the data, we computed the median and median absolute deviation per measurement of each model ln $\mathcal{L}$. Table 1 reports the resulting ln $\mathcal{L}$ ratio for various pairs of competing models, where each model ln $\mathcal{L}$ is calculated by scaling the median ln $\mathcal{L}$ per measurement from cross-validation to the full dataset size of 128 measurements. We find that the three-planet model is greatly favored over the two-planet model with a >8σ greater ln $\mathcal{L}$. Furthermore, the three-planet + GP model has a marginally better ln $\mathcal{L}$ than the three-planet model (i.e., 0.3σ higher ln $\mathcal{L}$). We, therefore, conclude that the more simplistic model with three Keplerian signals and no GP is most strongly favored based on the data. Although it favors the planet interpretation for GJ1132(d), we refrain from a definitive conclusion. As shown for previous examples from our survey, activity-induced Doppler shifts can indeed match a Keplerian signal (Bonfils et al. 2007).

The resulting RV model parameters, assuming that the observed RV variations are due to three planets plus residual stellar activity, which we modeled with a non-parametric GP, are reported in Table 2. GJ1132(d) is presented with parentheses around its d letter to stress that it is not accepted as a planet detection.

Table 2. Model parameters.

Parameter	Maximum a posteriori values with 16th and 84th percentiles		
Stellar parameters			
Stellar mass, M_s [$M_\odot$]	0.181 ± 0.019		
Stellar radius, R_s [$R_\odot$]	$0.2105^{+0.0102}_{-0.0085}$		
Stellar luminosity, L_s [$L_\odot$]	0.00438 ± 0.00034		
Effective temperature, $T_{\rm eff}$ [K]	3270 ± 140		
Rotation period, $P_{\rm rot}$ (days)	$122.3^{+6.0}_{-5.0}$		
Systemic velocity, γ_0 (m s^{-1})	35078.8 ± 0.8		
Gaussian process hyperparameters			
ln correlation amplitude, ln a (m s^{-1})	$-0.18^{+1.12}_{-1.32}$		
ln exponential timescale, ln λ (days)	$7.01^{+1.37}_{-1.31}$		
ln coherence parameter, ln Γ	$1.8^{+2.4}_{-5.4}$		
ln periodic timescale, ln $P_{\rm GP}$ (days)	$4.81^{1.79}_{-1.61}$		
Additive jitter, s (m s^{-1})	$0.19^{+0.63}_{-0.04}$		
	GJ1132b	GJ1132c	GJ1132(d)
Derived parameters			
Period, P (days)	1.628931 ± 0.000027	8.929 ± 0.010	176.9 ± 5.1
Time of inferior conjunction, T_0 [BJD-24 50 000]	7184.55786 ± 0.00031	7506.02 ± 0.34	$7496.8^{+14.4}_{-8.6}$
Radial velocity semi-amplitude, K (m s^{-1})	2.85 ± 0.34	2.57 ± 0.39	$3.03^{+0.58}_{-0.88}$
$h = \sqrt{e}\cos\omega$	0.05 ± 0.13	$-0.12^{+0.28}_{-0.25}$	$-0.10^{+0.27}_{-0.28}$
$k = \sqrt{e}\sin\omega$	-0.12 ± 0.25	0.14 ± 0.24	-0.05 ± 0.29
Calculated parameters			
Semi-major axis, a (AU)	0.0153 ± 0.0005	0.0476 ± 0.0017	0.35 ± 0.01
Eccentricity, e^a	<0.22	<0.27	<0.53
Planet mass, M_p [$M_\oplus$]	1.66 ± 0.23	–	–
Minimum planet mass, $M_p \sin i$ [$M_\oplus$]	1.66 ± 0.23	2.64 ± 0.44	$8.4^{+1.7}_{-2.5}$
Planet density, ρ_p (g cm^{-3})^b	6.3 ± 1.3	–	–
Surface gravity, g (m s^{-2})^b	12.9 ± 2.2	–	–
Escape velocity, $v_{\rm esc}$(km s^{-1})^b	13.6 ± 1.0	–	–
Equilibrium temperature, $T_{\rm eq}$ [K]			
Bond albedo of 0.3 (Earth-like)	529 ± 9	300 ± 5	111 ± 2
Bond albedo of 0.75 (Venus-like)	409 ± 7	232 ± 4	86 ± 1

Notes. Maximum a posteriori and 68.3% confidence intervals. Planets b and c are considered robust detections, but planet (d) is considered a planet candidate, but may also be the result of stellar activity. [(a)]Upper limit, 95th percentile of the posterior PDF. $M_\odot = 1.98842 \times 10^{30}$ kg, $R_\odot = 6.95508 \times 10^8$ m, $M_\oplus = 5.9736 \times 10^{24}$ kg, and $R_\oplus = 6\,378\,137$ m. [(b)]Assuming a planetary radius of $1.13 \pm 0.056\,R_\oplus$ (Dittmann et al. 2017a).

In the MCMC from which these results were derived we initialized 200 walkers and ran each chain for a duration of approximately 20 autocorrelation times to ensure adequate convergence of the chains. The steps corresponding to the first ~10 autocorrelation times were treated as the burn-in phase and discarded. The results are broadly consistent with the results from the iterative periodogram analysis of Sect. 3.1. The resulting marginalized posterior PDFs of the model parameters are shown in Fig. A.1.

As a complement, Figs. 3 and 4 show phase-folded RVs and residuals without the GP regression. The uncertainties are not rescaled. After removing the mean GP model and the best-fit Keplerians for GJ1132b and GJ1132c, the residual rms is 2.74 m s^{-1}.

4. Discussions

4.1. GJ1132b in context

Compared to the discovery paper, we revise the RV semi-amplitude from 2.76 ± 0.92 to 2.85 ± 0.34 m s^{-1}. This is a faster gain in precision than expected from the larger number of RVs ($0.92/0.34 > \sqrt{128/25}$). We surmise this is because a three-planet model is a more adequate description of the data. This improves the mass precision by ~2.4× from 1.62 ± 0.55 to 1.66 ± 0.23 $M_\oplus$. Together with the radius of GJ1132b measured by Dittmann et al. (2017a), its bulk density then becomes 6.3 ± 1.3 g cm^{-3} and thus confirms its rocky nature.

The mass-period diagram (Fig. 5) places GJ1132b in context and compares its mass and radius with other transit detections and with theoretical curves for different bulk compositions (Zeng & Sasselov 2013). The density of GJ1132b appears compatible with a rocky or a denser compositions. With such a diagram, Rogers (2015) observed that below ~1.6 $R_\oplus$, planets are predominantly rocky, that is to say, they are preferentially found below the mass-radius curves that include significant water or lighter elements in their composition. The largest planet that is more than 1σ away from the rocky curve is indeed Kepler-60b, with a radius of 1.7 $R_\oplus$ (Steffen et al. 2013; Jontof-Hutter et al. 2016).

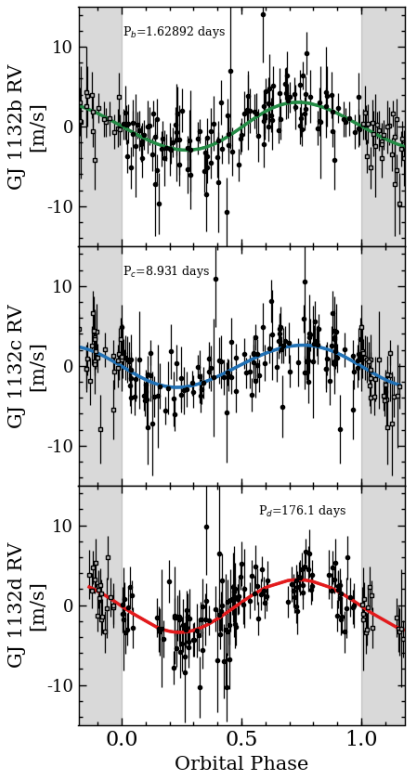

Fig. 3. Phase-folded RV decomposition for the three-planet model without GP regression.

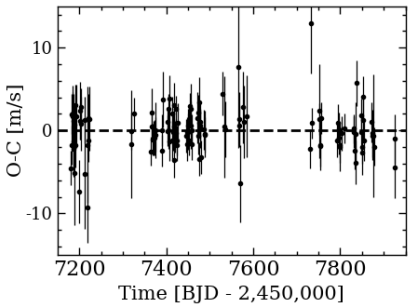

Fig. 4. RV residuals (O−C) as a function of time.

Conversely, a similar threshold can now be observed with mass: with the exception of three planets with very large uncertainties (Kepler -11b, -11f, and -177b; Lissauer et al. 2011, 2013; Xie 2014), no planet is seen to lie not on the rocky curve by more than 1σ below a mass threshold of $\sim 3\ M_\oplus$.

4.2. GJ1132c, a temperate super-Earth

With a host star luminosity $L_\star = 0.00438 \pm 0.00034\ L_\odot$ (Dittmann et al. 2017b) and a semi-major $a = 0.048$ AU, GJ1132c receives about 1.9 times as much flux as Earth from our Sun. Its equilibrium temperature ranges from 232 K for a Bond albedo equal to that of Venus ($A = 0.75$) and up to 328 K for a Bond albedo $A = 0$.

The most recent works that delineated the habitable zone around M dwarfs (e.g., Kopparapu et al. 2016) place the inner edge for GJ1132 at about 1.6 times the stellar radiation received by Earth. GJ1132c would thus be considered significantly too irradiated to have liquid water on its surface. The planet still remains of considerable interest in the context of habitability. The concept remains poorly understood and will remain so until inhabited worlds are actually found. The inner edge of the habitable zone is thus subject to change with future works. Moreover, if future instrumentation were able to reach sufficient contrast for resolving the planet from its parent star, probing for an atmosphere would tell us how resilient this atmosphere can be against stellar irradiation, and thus would more generally constrain the habitability of M-dwarf planets regardless of the habitability of GJ1132c itself. At a distance of 12 parsec, however (Berta-Thompson et al. 2015), transmission and occultation spectroscopy are probably the only methods able to resolve such an atmosphere, meaning that GJ1132c would be required to transit.

4.3. Transit search for planet c

The source GJ1132c orbits at a distance of about $49 \pm 3\ R_\star$ from its host star, and without prior knowledge on the system orientation, the probability of detecting the planet in transit at inferior conjunction would be ~1/50. We nevertheless have prior knowledge on the system orientation since GJ1132 is already known to host a transiting planet with a measured orbital inclination of $88.68^{+0.40}_{-0.33}$ degrees (Dittmann et al. 2017a). Considering only this nominal value (88.68 degrees), additional planets with strictly coplanar orbits would be seen to transit up to separations of $\sim 43\ R_\star$, and would be missed beyond. This limit is most probably inside the orbit of GJ1132c, and at first, the prior knowledge we have from GJ1132b might be thought to nullify the probability of observing any transit for GJ1132c. This neglects both the uncertainty on the orbital inclination of GJ1132c and possible deviations from perfect coplanarity, however.

We can instead include both uncertainty and non-coplanarity in our prior. Using the formalism of Beatty & Seager (2010), we distributed inclinations centered around 88.68 degrees with various standard deviations. In Fig. 6, we show that the prior probability that GJ1132c undergoes transit quickly jumps to ~43% for inclinations distributed with only a small standard deviation of 1 degree.

From our analysis in Sect. 3, we derived an ephemeris for the passage of GJ1132c at inferior conjunction (BJD = 2457506.02 ± 0.34). Figure 7 shows that this falls inside the long 100 h monitoring made by Dittmann et al. (2017a) with *Spitzer*, which covers epochs between BJD = 2457502.5 and 2457506.8 almost without interruption and a sensitivity down to planets smaller than Mars (Dittmann et al. 2017a). Possible transits of GJ1132c are largely ruled out with a <1% chance that an existing transit was missed.

The prior probability combined with the probability left by the incomplete coverage of the transit-time window gives a posterior probability ≤0.43% that GJ1132c undergoes transits[1]. GJ1132c transits are almost completely ruled out.

4.4. Stellar activity or a cold planet

Based on activity diagnostics, we were not able to rule out stellar activity as the main cause of the 170 d RV periodicity. However, if later observations were to confirm the planetary nature of this signal, GJ1132(d) would have a minimum mass $m_d \sin i = 8.4^{+1.7}_{-2.5}\ M_\oplus$, which is in the mass domain between super-Earths and mini-Neptunes. Its semi-major axis $a_d = 0.35 \pm 0.01$ AU would place this planet beyond the ice line, with an equilibrium temperature of 86 K (111 K) for a Bond albedo

[1] 0.43% is the upper limit considering a standard deviation of 1 degree in our above calculations, and for all other standard deviations, the posterior probability is lower than 0.43%.

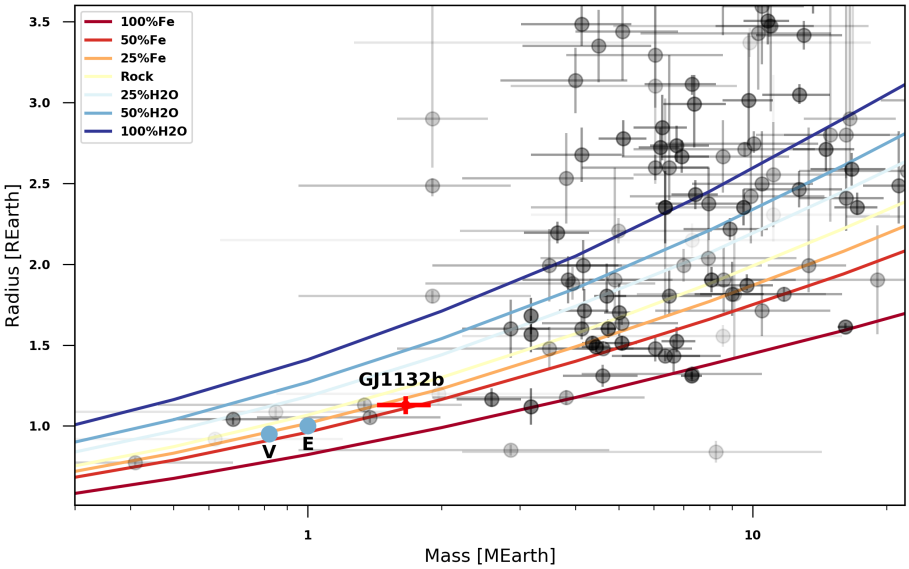

Fig. 5. Mass–radius diagram for planets with masses $M_p < 20$ $M_\oplus$ and radii $R_p < 3.5$ $R_\oplus$ queried from the NASA Exoplanet Archive. The gray level scales linearly with the relative uncertainties (with equal weight for both mass and radius). GJ1132b is shown in red, and blue circles show Earth and Venus. Curves are for the mass–radius relations predicted with theoretical models (Zeng & Sasselov 2013).

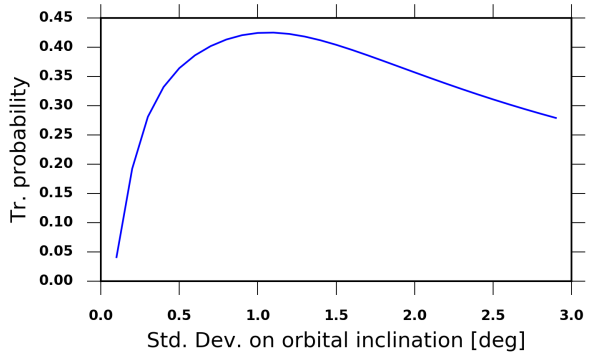

Fig. 6. Transit probability of GJ1132c with a Gaussian prior on inclination. We chose the inclination of planet b for the central value of the distribution (i_b = 88.68 degrees), and we computed the transit probability for various standard deviations of this distribution (x axis) to reflect both the uncertainty on i_b and a small possible non-coplanarity.

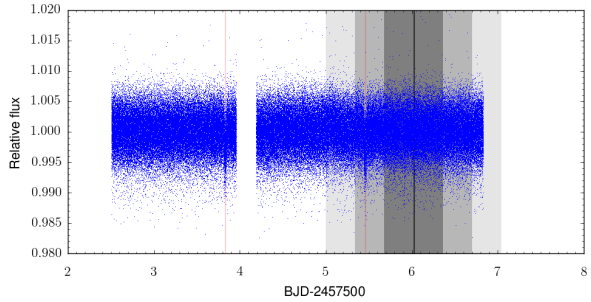

Fig. 7. Ephemerides for the GJ1132c inferior conjunction overplotted on *Spitzer* photometry. Based on this data set, Dittmann et al. (2017a) excluded possible transits of any additional planet larger than Mars. GJ1132c transits are therefore largely excluded.

of 0.75 (0.3). Planet d would be ∼7.3 times farther away from the star than planet c. A priori, its transit probability would thus be ∼7.3 lower. *Spitzer* photometry rejects only a small portion (13%) of possible transit configurations.

4.5. Transit-timing variations

The orbital period ratio of planets b and c is close to 11/2. Even if inside a resonance, its low order would imply low transit-timing variations (TTV). We use the `Rebound` code (Rein & Liu 2011) with the `WHFast` integrator (Rein & Tamayo 2015) to compute TTVs for this system. Although not shown here, TTVs were found to be generally lower than 30 s, in agreement with the lack of TTVs found in Dittmann et al. (2017a).

5. Conclusion

To conclude, our HARPS RV follow-up helps to describe the GJ1132 system more completely and with more details. We confirm the detection of planet b based on RVs alone, and we refine its characteristics, including its mass, density, and eccentricity. We also detect at least one new planet in the system. Assuming coplanarity with planet b, GJ1132c is a super-Earth with mass $m_c = 2.75^{+0.76}_{-0.61}$ $M_\oplus$. Its equilibrium temperature is that of a temperate planet, although it is probably too close to the star to allow for liquid water on its surface. Finally, we also detect a third Keplerian signal, but its true nature is yet to be decided (planet or stellar activity). If confirmed as a planet, GJ1132(d) would be a super-Earth or mini-Neptune found farther away from the star and beyond the ice line. Further observations, and potentially at other wavelengths with infrared spectrographs such as CARMENES (Quirrenbach et al. 2014; Sarkis et al. 2018) or SPIROU (Delfosse et al. 2013), may help to interpret the true nature of this signal.

Acknowledgements. We are grateful to our referee for comments that significantly improved our manuscript. X.B., J.M.A., and A.W. acknowledge funding from the European Research Council under the ERC Grant Agreement n. 337591-ExTrA. R.C. and R.D. acknowledge financial support from the National Research Council of Canada and the Institute for Research on Exoplanets. N.A-D. acknowledges support from FONDECYT #3180063. N.C.S. acknowledges the support by Fundação para a Ciência e a Tecnologia (FCT, Portugal) through the research grant through national funds and by FEDER through COMPETE2020 by grants UID/FIS/04434/2013&POCI-01-0145-FEDER-007672 and PTDC/FIS-AST/1526/2014&POCI-01-0145-FEDER-016886, as well as through Investigador FCT contract nr. IF/00169/2012/CP0150/CT0002. J.A.D. gratefully acknowledges funding from the Heising-Simons Foundation's 51 Pegasi b postdoctoral fellowship. E.R.N. is supported by an NSF Astronomy and Astrophysics Postdoctoral Fellowship under award AST-1602597. The MEarth Team gratefully acknowledges funding from the David and Lucille Packard Fellowship for Science and Engineering (awarded to D.C.). This material is based upon work supported by the National Science Foundation under grants AST-0807690, AST-1109468, AST-1004488 (Alan T. Waterman Award), and AST-1616624. E.R.N. is supported by an NSF Astronomy and Astrophysics Postdoctoral Fellowship. This publication was made possible through the support of a grant from the

John Templeton Foundation. The opinions expressed in this publication are those of the authors and do not necessarily reflect the views of the John Templeton Foundation. This research has made use of the NASA Exoplanet Archive, which is operated by the California Institute of Technology, under contract with the National Aeronautics and Space Administration under the Exoplanet Exploration Program.

References

Anglada-Escudé, G., & Butler, R. P. 2012, Camb. Astrophys. Ser., 20, 15
Arlot, S., & Celisse, A. 2010, Statist. Surv., 4, 40
Astudillo-Defru, N., Bonfils, X., Delfosse, X., et al. 2015, A&A, 575, A119
Astudillo-Defru, N., Delfosse, X., Bonfils, X., et al. 2017, A&A, 600, A13
Baranne, A., Queloz, D., Mayor, M., et al. 1996, A&AS, 119, 373
Beatty, T. G., & Seager, S. 2010, ApJ, 712, 1433
Berta-Thompson, Z. K., Irwin, J., Charbonneau, D., et al. 2015, Nature, 527, 204
Boisse, I., Eggenberger, A., Santos, N. C., et al. 2010, A&A, 523, A88
Bonfils, X., Mayor, M., Delfosse, X., et al. 2007, A&A, 474, 293
Bonfils, X., Astudillo-Defru, N., Díaz, R., et al. 2018, A&A, 613, A25
Bouchy, F., Pepe, F., & Queloz, D. 2001, A&A, 374, 733
Cloutier, R., Astudillo-Defru, N., Doyon, R., et al. 2017a, A&A, 608, A35
Cloutier, R., Doyon, R., Menou, K., et al. 2017b, AJ, 153, 9
Delfosse, X., Donati, J.-F., Kouach, D., et al. 2013, in SF2A-2013: Proceedings of the Annual meeting of the French Society of Astronomy and Astrophysics, ed., L. Cambresy, 497
Dittmann, J. A., Irwin, J. M., Charbonneau, D., Berta-Thompson, Z. K., & Newton, E. R. 2017a, AJ, 154, 142
Dittmann, J. A., Irwin, J. M., Charbonneau, D., et al. 2017b, Nature, 544, 333
Donati, J.-F., Yu, L., Moutou, C., et al. 2016, MNRAS, 465, 3343
Ford, E. B. 2006, ApJ, 642, 505
Foreman-Mackey, D., Conley, A., Meierjurgen Farr, W., et al. 2013, Astrophysics Source Code Library [record ascl:1303.002]
Galland, F., Lagrange, A. M., Udry, S., et al. 2006, A&A, 447, 355
Gillon, M., Bonfils, X., Demory, B.-O., et al. 2011, A&A, 525, A32
Gillon, M., Triaud, A. H. M. J., Demory, B.-O., et al. 2017, Nature, 542, 456
Gomes da Silva, J., Santos, N. C., Bonfils, X., et al. 2011, A&A, 534, A30
Goodman, J., & Weare, J. 2010, Commun. Appl. Math. Comput. Sci., 5, 65
Haywood, R. D., Collier Cameron, A., Queloz, D., et al. 2014, MNRAS, 443, 2517
Howarth, I. D., Siebert, K. W., Hussain, G. A. J., & Prinja, R. K. 1997, MNRAS, 284, 265
Jontof-Hutter, D., Ford, E. B., Rowe, J. F., et al. 2016, ApJ, 820, 39
Kopparapu, R. k., Wolf, E. T., Haqq-Misra, J., et al. 2016, ApJ, 819, 84
Lissauer, J. J., Fabrycky, D. C., Ford, E. B., et al. 2011, Nature, 470, 53
Lissauer, J. J., Jontof-Hutter, D., Rowe, J. F., et al. 2013, ApJ, 770, 131
Lovis, C., & Pepe, F. 2007, A&A, 468, 1115
Mayor, M., Pepe, F., Queloz, D., et al. 2003, The Messenger, 114, 20
Morley, C. V., Kreidberg, L., Rustamkulov, Z., Robinson, T., & Fortney, J. J. 2017, ApJ, 850, 121
Pepe, F., Mayor, M., Galland, F., et al. 2002, A&A, 388, 632
Pepe, F., Mayor, M., Queloz, D., et al. 2004, A&A, 423, 385
Press, W. H., Teukolsky, S. A., Vetterling, W. T., & Flannery, B. P. 1992, Numerical Recipes (New York: Cambridge University Press)
Quirrenbach, A., Amado, P. J., Caballero, J. A., et al. 2014, Proc. SPIE, 9147, 91471F
Rajpaul, V., Aigrain, S., Osborne, M. A., Reece, S., & Roberts, S. 2015, MNRAS, 452, 2269
Rein, H., & Liu, S.-F. 2011, Astrophysics Source Code Library [record ascl:1110.016]
Rein, H., & Tamayo, D. 2015, MNRAS, 452, 376
Robertson, P., Mahadevan, S., Endl, M., & Roy, A. 2014, Science, 345, 440
Rogers, L. A. 2015, ApJ, 801, 41
Sarkis, P., Henning, T., Kürster, M., et al. 2018, AJ, 155, 257
Schaefer, L., Wordsworth, R. D., Berta-Thompson, Z., & Sasselov, D. 2016, ApJ, 829, 63
Southworth, J., Mancini, L., Madhusudhan, N., et al. 2017, AJ, 153, 191
Steffen, J. H., Fabrycky, D. C., Agol, E., et al. 2013, MNRAS, 428, 1077
Xie, J.-W. 2014, APJS, 210, 25
Zechmeister, M., & Kürster, M. 2009, A&A, 496, 577
Zeng, L., & Sasselov, D. 2013, PASP, 125, 227

Appendix A: Additional figure and table

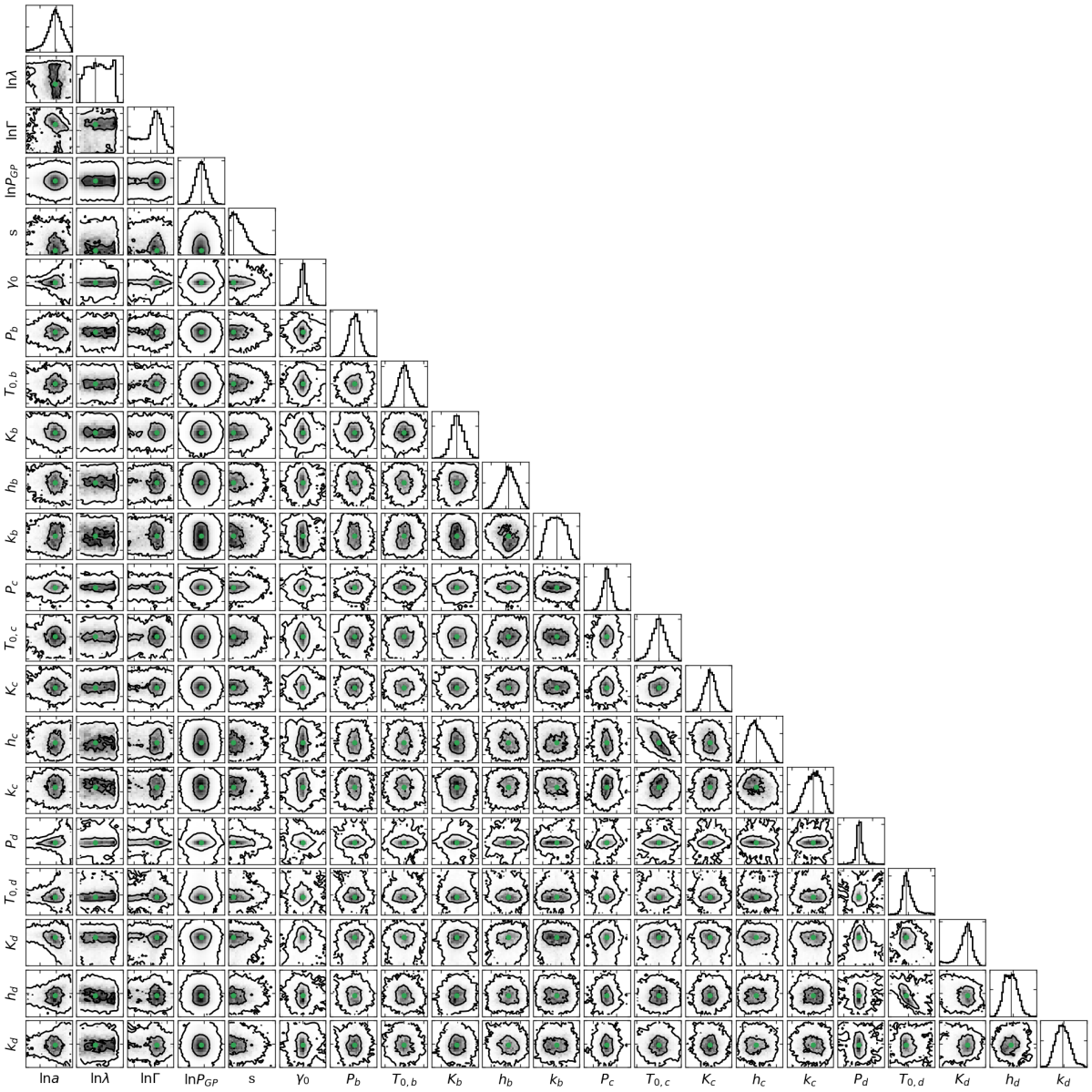

Fig. A.1. Marginal posterior PDFs of the model parameters. See text for details.

Table A.1. HARPS RV and spectroscopic index time-series.

BJD-2400000.0	RV (km s^{-1})	σRV (km s^{-1})	H_α	σH_α	H_β	σH_β	NaD	σNaD	S	σS
57180.4657	35.0715	0.0021	0.0736	0.0002	0.0594	0.0006	0.0078	0.0002	1.1837	0.1395
57181.4875	35.0777	0.0024	0.0737	0.0003	0.0593	0.0008	0.0073	0.0003	1.2959	0.1978
57182.5211	35.0790	0.0024	0.0738	0.0003	0.0604	0.0008	0.0072	0.0003	1.1192	0.2717
57183.5369	35.0766	0.0029	0.0733	0.0003	0.0628	0.0010	0.0075	0.0004	1.0605	0.2463
57184.5827	35.0770	0.0034	0.0746	0.0004	0.0623	0.0013	0.0081	0.0005	1.3121	0.4228
57185.4828	35.0725	0.0034	0.0774	0.0004	0.0697	0.0012	0.0083	0.0005	1.1838	0.2943
57186.4758	35.0688	0.0034	0.0789	0.0004	0.0730	0.0012	0.0090	0.0005	1.0703	0.3002
57187.4707	35.0770	0.0033	0.0739	0.0004	0.0611	0.0011	0.0076	0.0005	1.2266	0.2843
57188.4751	35.0677	0.0063	0.0759	0.0007	0.0639	0.0023	0.0077	0.0011	0.5631	0.5589
57189.4766	35.0767	0.0024	0.0737	0.0003	0.0620	0.0009	0.0079	0.0003	1.3587	0.3760
57190.4747	35.0828	0.0025	0.0757	0.0003	0.0666	0.0009	0.0087	0.0003	1.1962	0.2160
57191.4635	35.0733	0.0026	0.0726	0.0003	0.0579	0.0008	0.0072	0.0003	1.0801	0.2145
57192.4695	35.0811	0.0038	0.0756	0.0004	0.0667	0.0012	0.0093	0.0006	1.2518	0.3017
57199.4737	35.0686	0.0039	0.0759	0.0003	0.0692	0.0008	0.0149	0.0003	0.8405	0.2049
57200.4709	35.0826	0.0022	0.0730	0.0003	0.0646	0.0007	0.0076	0.0002	1.1800	0.1595
57201.4700	35.0781	0.0035	0.0759	0.0004	0.0736	0.0013	0.0108	0.0004	0.8145	0.3528
57203.4724	35.0772	0.0033	0.0767	0.0004	0.0679	0.0010	0.0097	0.0004	2.0155	0.2546
57204.4690	35.0739	0.0022	0.0732	0.0003	0.0602	0.0007	0.0088	0.0002	0.6547	0.1638
57211.4898	35.0786	0.0028	0.1089	0.0004	0.1535	0.0014	0.0181	0.0004	3.7218	0.3768
57212.4771	35.0678	0.0065	0.0759	0.0007	0.0694	0.0025	0.0085	0.0010	3.5179	4.3547
57218.4902	35.0808	0.0070	0.0774	0.0007	0.0719	0.0027	0.0072	0.0012	2.6520	1.2886
57219.4812	35.0686	0.0043	0.0766	0.0005	0.0763	0.0016	0.0071	0.0006	1.3183	0.6870
57220.4694	35.0780	0.0029	0.0751	0.0003	0.0669	0.0010	0.0074	0.0003	0.9122	0.3073
57221.4706	35.0769	0.0025	0.0769	0.0003	0.0660	0.0009	0.0079	0.0003	1.3581	0.3381
57222.4842	35.0738	0.0039	0.0784	0.0004	0.0762	0.0016	0.0109	0.0005	2.8997	0.6544
57318.8586	35.0770	0.0022	0.0778	0.0003	0.0709	0.0007	0.0101	0.0002	1.4137	0.1460
57319.8553	35.0739	0.0065	0.0747	0.0007	0.0550	0.0022	0.0090	0.0010	0.9849	0.9136
57325.8585	35.0855	0.0019	0.0747	0.0002	0.0637	0.0006	0.0084	0.0002	1.3391	0.0847
57364.8062	35.0725	0.0017	0.0732	0.0002	0.0567	0.0005	0.0053	0.0001	0.8243	0.0849
57365.8194	35.0703	0.0016	0.0736	0.0002	0.0563	0.0004	0.0057	0.0001	0.7972	0.0720
57366.7942	35.0782	0.0029	0.0739	0.0003	0.0582	0.0008	0.0057	0.0003	0.8061	0.1615
57367.8072	35.0745	0.0020	0.0734	0.0002	0.0551	0.0005	0.0057	0.0002	0.8998	0.1020
57370.8365	35.0741	0.0021	0.0721	0.0002	0.0564	0.0006	0.0065	0.0002	1.0348	0.1061
57371.8364	35.0755	0.0022	0.0736	0.0003	0.0577	0.0006	0.0060	0.0002	0.6316	0.1142
57373.8390	35.0704	0.0034	0.0740	0.0004	0.0571	0.0009	0.0059	0.0004	0.6013	0.1954
57374.7626	35.0756	0.0020	0.0746	0.0002	0.0601	0.0006	0.0072	0.0002	0.9275	0.1048
57389.8172	35.0778	0.0019	0.0740	0.0002	0.0606	0.0005	0.0064	0.0002	0.8959	0.0829
57390.8011	35.0757	0.0019	0.0740	0.0002	0.0616	0.0005	0.0065	0.0002	0.9732	0.0809
57391.8098	35.0764	0.0034	0.0741	0.0004	0.0585	0.0010	0.0071	0.0004	0.3834	0.2935
57401.7321	35.0757	0.0015	0.0752	0.0002	0.0649	0.0004	0.0075	0.0001	1.1823	0.0609
57403.7974	35.0823	0.0019	0.0764	0.0002	0.0685	0.0005	0.0083	0.0002	1.3221	0.0755
57404.7412	35.0796	0.0022	0.0790	0.0003	0.0730	0.0007	0.0083	0.0002	1.4257	0.1107
57405.6930	35.0881	0.0017	0.0751	0.0002	0.0677	0.0005	0.0082	0.0002	1.2337	0.0754
57406.7642	35.0841	0.0028	0.0754	0.0003	0.0681	0.0009	0.0077	0.0003	1.4073	0.1748
57407.6980	35.0793	0.0024	0.0737	0.0002	0.0505	0.0045	0.0080	0.0003	-1.8703	3.2426
57412.7474	35.0790	0.0023	0.0757	0.0003	0.0635	0.0007	0.0085	0.0002	0.9553	0.1079
57413.7202	35.0876	0.0019	0.0733	0.0002	0.0627	0.0006	0.0086	0.0002	1.1364	0.0899
57415.7809	35.0830	0.0022	0.0772	0.0003	0.0704	0.0007	0.0089	0.0002	1.6911	0.1186
57416.7217	35.0842	0.0027	0.0737	0.0003	0.0656	0.0008	0.0076	0.0003	1.3785	0.1412
57417.7195	35.0773	0.0023	0.0763	0.0003	0.0693	0.0007	0.0083	0.0002	1.6400	0.1145
57418.7193	35.0775	0.0021	0.0742	0.0002	0.0663	0.0006	0.0084	0.0002	1.3759	0.1162
57420.7413	35.0797	0.0019	0.0929	0.0003	0.1135	0.0007	0.0137	0.0002	2.6172	0.1104
57421.7295	35.0863	0.0016	0.0740	0.0002	0.0647	0.0005	0.0078	0.0001	1.1015	0.0828
57422.7158	35.0802	0.0017	0.0797	0.0002	0.0772	0.0005	0.0102	0.0002	1.8171	0.0822
57423.7243	35.0843	0.0019	0.0778	0.0002	0.0739	0.0006	0.0096	0.0002	1.7806	0.1194

Notes. Radial velocities are given in the solar system barycentric reference frame.

Table A.1. continued.

BJD-2400000.0	RV (km s^{-1})	σRV (km s^{-1})	H_α	σH_α	H_β	σH_β	NaD	σNaD	S	σS
57424.6908	35.0800	0.0018	0.0734	0.0002	0.0627	0.0005	0.0080	0.0002	1.2936	0.0928
57425.6801	35.0815	0.0024	0.0744	0.0003	0.0640	0.0007	0.0080	0.0003	1.6742	0.1567
57446.6185	35.0818	0.0020	0.0798	0.0002	0.0753	0.0006	0.0102	0.0002	1.4571	0.0769
57447.6264	35.0804	0.0021	0.0772	0.0003	0.0716	0.0006	0.0098	0.0002	1.6056	0.0810
57448.5920	35.0821	0.0019	0.0764	0.0002	0.0691	0.0006	0.0085	0.0002	1.5313	0.0688
57449.5756	35.0875	0.0022	0.1053	0.0003	0.1542	0.0010	0.0171	0.0003	2.6527	0.0831
57450.5911	35.0831	0.0021	0.0754	0.0002	0.0693	0.0006	0.0084	0.0002	1.1410	0.0705
57451.5918	35.0841	0.0018	0.0733	0.0002	0.0640	0.0005	0.0079	0.0002	1.1318	0.0719
57452.5529	35.0839	0.0018	0.0819	0.0002	0.0872	0.0006	0.0099	0.0002	1.8971	0.0765
57453.5449	35.0816	0.0016	0.0742	0.0002	0.0654	0.0005	0.0084	0.0001	1.3474	0.0716
57455.7948	35.0818	0.0028	0.0759	0.0003	0.0679	0.0010	0.0086	0.0003	1.2791	0.3333
57456.5705	35.0851	0.0030	0.0760	0.0003	0.0674	0.0010	0.0091	0.0004	1.4816	0.2336
57457.5540	35.0837	0.0019	0.0742	0.0002	0.0654	0.0006	0.0082	0.0002	1.4374	0.0909
57458.5628	35.0821	0.0019	0.0735	0.0002	0.0658	0.0006	0.0081	0.0002	1.2384	0.0941
57470.6955	35.0846	0.0031	0.0721	0.0004	0.0588	0.0009	0.0093	0.0004	0.7902	0.1269
57472.7555	35.0793	0.0022	0.0751	0.0003	0.0670	0.0007	0.0081	0.0002	0.8746	0.1102
57473.5981	35.0805	0.0021	0.0740	0.0002	0.0638	0.0006	0.0081	0.0002	1.0454	0.1138
57474.6150	35.0808	0.0017	0.0724	0.0002	0.0605	0.0005	0.0069	0.0002	0.9109	0.0870
57475.6271	35.0885	0.0030	0.0723	0.0004	0.0620	0.0008	0.0072	0.0004	0.9834	0.1501
57476.6011	35.0770	0.0020	0.0753	0.0002	0.0642	0.0006	0.0080	0.0002	1.3693	0.1018
57477.5256	35.0855	0.0024	0.0762	0.0003	0.0652	0.0007	0.0082	0.0003	2.1576	0.1534
57477.6036	35.0853	0.0019	0.0767	0.0002	0.0679	0.0006	0.0087	0.0002	1.4413	0.1070
57478.6655	35.0835	0.0022	0.0724	0.0002	0.0600	0.0006	0.0065	0.0002	1.2298	0.1417
57479.6303	35.0742	0.0020	0.0738	0.0002	0.0619	0.0006	0.0068	0.0002	1.7087	0.1287
57486.5663	35.0803	0.0024	0.0767	0.0003	0.0711	0.0008	0.0080	0.0003	1.3607	0.1315
57488.5522	35.0801	0.0021	0.0726	0.0003	0.0602	0.0006	0.0070	0.0002	0.9245	0.0871
57488.7183	35.0808	0.0028	0.0731	0.0003	0.0622	0.0009	0.0070	0.0003	1.3646	0.1755
57529.5196	35.0866	0.0027	0.0739	0.0003	0.0632	0.0008	0.0083	0.0003	0.9024	0.1630
57533.5194	35.0734	0.0061	0.0816	0.0007	0.0760	0.0022	0.0114	0.0011	1.1707	0.4517
57536.5792	35.0743	0.0033	0.0802	0.0004	0.0881	0.0013	0.0097	0.0005	1.4100	0.2996
57566.4667	35.0868	0.0098	0.0723	0.0010	0.0665	0.0041	0.0090	0.0019	1.2531	0.6473
57567.4772	35.0788	0.0025	0.0758	0.0003	0.0740	0.0009	0.0094	0.0003	1.5649	0.2308
57568.4726	35.0819	0.0033	0.0747	0.0003	0.0719	0.0013	0.0095	0.0005	1.2613	0.3376
57569.5552	35.0673	0.0047	0.0743	0.0005	0.0709	0.0019	0.0085	0.0008	1.5105	0.4358
57576.5030	35.0850	0.0044	0.0803	0.0005	0.0746	0.0016	0.0092	0.0007	1.3251	0.2503
57577.5167	35.0769	0.0044	0.0735	0.0004	0.0637	0.0017	0.0087	0.0007	1.4878	0.6083
57584.5054	35.0840	0.0049	0.0731	0.0005	0.0687	0.0019	0.0088	0.0008	0.6917	0.3945
57729.8316	35.0752	0.0023	0.0730	0.0003	0.0620	0.0007	0.0076	0.0002	1.1951	0.1406
57732.8377	35.0890	0.0060	0.0779	0.0007	0.0654	0.0020	0.0085	0.0009	1.5138	0.9210
57734.8518	35.0813	0.0019	0.0734	0.0002	0.0628	0.0005	0.0075	0.0002	1.2762	0.0887
57751.7936	35.0771	0.0019	0.0724	0.0002	0.0620	0.0006	0.0081	0.0002	1.2669	0.1141
57752.8122	35.0847	0.0057	0.0729	0.0006	0.0644	0.0019	0.0075	0.0009	1.1037	0.4191
57753.8014	35.0781	0.0030	0.0724	0.0003	0.0642	0.0009	0.0084	0.0004	1.2188	0.2001
57754.8207	35.0770	0.0024	0.0723	0.0003	0.0621	0.0007	0.0078	0.0003	1.1402	0.1332
57755.8231	35.0831	0.0019	0.0751	0.0002	0.0682	0.0006	0.0091	0.0002	1.3481	0.1158
57792.7277	35.0751	0.0020	0.0764	0.0002	0.0728	0.0006	0.0092	0.0002	1.3278	0.1112
57795.6726	35.0782	0.0022	0.0743	0.0003	0.0647	0.0006	0.0096	0.0002	1.0836	0.0807
57796.6455	35.0843	0.0021	0.0829	0.0003	0.0810	0.0007	0.0110	0.0002	1.6221	0.0927
57797.6402	35.0795	0.0019	0.0716	0.0002	0.0591	0.0005	0.0078	0.0002	1.0547	0.0885
57798.6965	35.0809	0.0021	0.0727	0.0002	0.0605	0.0006	0.0085	0.0002	1.1639	0.0922
57799.6246	35.0818	0.0030	0.0719	0.0003	0.0581	0.0008	0.0088	0.0004	1.1241	0.1988
57803.7585	35.0763	0.0021	0.0729	0.0002	0.0614	0.0006	0.0082	0.0002	1.1774	0.1587
57810.6343	35.0769	0.0018	0.0746	0.0002	0.0709	0.0005	0.0082	0.0002	1.4949	0.0846
57830.5833	35.0794	0.0019	0.0803	0.0002	0.0830	0.0006	0.0099	0.0002	1.9467	0.1141
57831.5423	35.0770	0.0017	0.0736	0.0002	0.0662	0.0005	0.0080	0.0002	1.1967	0.1104
57832.5735	35.0811	0.0022	0.0761	0.0003	0.0698	0.0007	0.0084	0.0002	1.5973	0.1742
57834.5604	35.0775	0.0026	0.0751	0.0003	0.0694	0.0008	0.0093	0.0003	1.5597	0.2012
57835.5218	35.0825	0.0038	0.0836	0.0004	0.0830	0.0014	0.0115	0.0006	1.5755	0.3235

Table A.1. continued.

BJD-2400000.0	RV (km s^{-1})	σRV (km s^{-1})	H_α	σH_α	H_β	σH_β	NaD	σNaD	S	σS
57836.5391	35.0818	0.0028	0.0743	0.0003	0.0664	0.0009	0.0079	0.0004	1.3216	0.2138
57847.6649	35.0737	0.0023	0.0749	0.0003	0.0661	0.0007	0.0084	0.0002	1.2955	0.2598
57848.7030	35.0808	0.0021	0.0758	0.0002	0.0659	0.0007	0.0086	0.0002	2.0690	0.3198
57849.7216	35.0725	0.0026	0.0755	0.0003	0.0682	0.0009	0.0084	0.0003	1.1287	0.4710
57850.5931	35.0790	0.0020	0.0771	0.0002	0.0702	0.0006	0.0098	0.0002	1.4973	0.1231
57851.7008	35.0822	0.0026	0.0755	0.0003	0.0657	0.0009	0.0091	0.0003	1.1375	0.2224
57852.6557	35.0815	0.0025	0.0788	0.0003	0.0770	0.0009	0.0100	0.0003	1.0996	0.2015
57854.6927	35.0733	0.0026	0.0764	0.0003	0.0674	0.0009	0.0101	0.0003	1.0953	0.1944
57872.5444	35.0741	0.0024	0.0726	0.0003	0.0618	0.0007	0.0076	0.0003	1.1265	0.1617
57873.6706	35.0727	0.0029	0.0735	0.0003	0.0637	0.0011	0.0074	0.0004	0.9222	0.3373
57874.5623	35.0746	0.0030	0.0783	0.0003	0.0736	0.0010	0.0097	0.0004	1.4706	0.2621
57875.6886	35.0714	0.0074	0.0747	0.0008	0.0614	0.0031	0.0086	0.0013	1.3750	0.7009
57877.5748	35.0749	0.0023	0.0734	0.0003	0.0613	0.0008	0.0080	0.0003	1.1110	0.2208
57924.5360	35.0747	0.0030	0.0737	0.0003	0.0620	0.0011	0.0078	0.0004	2.0765	0.3792
57925.5331	35.0745	0.0037	0.0774	0.0004	0.0698	0.0014	0.0091	0.0005	1.8617	0.4392